Journal of Materials Chemistry C

ROYAL SOCIETY OF CHEMISTRY

COMMUNICATION

View Article Online
View Journal | View Issue

Cite this: J. Mater. Chem. C, 2021, 9, 17313

Received 28th September 2021,
Accepted 13th November 2021

DOI: 10.1039/d1tc04651a

rsc.li/materials-c

Pressure-dependent topographic evolutions of cold-sintered zinc oxide surfaces†

Sun Hwi Bang * and Clive A. Randall

By applying atomic force microscope to the flat in-plane polycrystalline microstructure, pressure-dependent topographic evolutions can be studied with respect to surface dihedral angle and groove geometry. Using a cold-sintered zinc oxide densified at 200 °C as a model system, this study demonstrates an experimental methodology for the quantification of relative grain boundary energetics in cold-sintered material systems and an associated geometric model for connecting the morphological change and underlying mechanochemical phenomenon at various uniaxial pressures ranging from 70 to 475 MPa. Depending on the applied pressure, the anisotropic grain growth, normal grain growth, and coarsening of particles are distinctively observed according to the changes in the groove geometry, suggesting that the growth kinetics can be considered as a function of pressure.

Zinc oxide (ZnO) is a versatile material used in a wide range of functional applications and present in various sizes and forms.[1,2] This n-type semiconductor material has a melting point of 1975 °C,[3] indicating that a high sintering temperature is necessary to densify it into a bulk and polycrystalline form. However, the recent advances in the cold sintering process have revealed that ZnO and other material systems can be highly densified at substantially low temperatures.[4–6] Considering that the homologous temperature of solid-state sintering is generally around 0.70 to drive atomic diffusion, the cold sintering only requires 0.20 or below to enable a powder densification. Such a low-temperature process is governed by dissolution and precipitation, enabling a transient liquid phase under uniaxial pressure and heat, where its mechanochemical process closely resembles the diffusive mass transfer of the pressure solution creep.[7,8] In fact, the time scale of the cold sintering is radically faster than the length of the geologic phenomenon but fluid-enhanced dissolution at grain contacts and precipitation at pores occur comparably in both processes.

Materials Research Institute and Department of Materials Science and Engineering, Pennsylvania State University, University Park, PA, 16802, USA.
E-mail: sbang@psu.edu

† Electronic supplementary information (ESI) available. See DOI: 10.1039/d1tc04651a

Innovating a low-temperature sintering is directly related to reducing the environmental footprint and also opens new opportunities in material discovery.[9,10] Although the research, technological and societal values of the cold sintering process have been comprehensively elucidated and resonated among diverse scientific communities, understanding of its fundamental sintering mechanism is rather limited especially in associated mechanochemical evolutions[11] and localized characterizations.[12] Hence, this study proposes (1) a method of preserving the in-plane surface (perpendicular to the axial direction) microstructure to characterize the topographic evolutions of cold-sintered ZnO and (2) an associated geometric model to understand the surface morphological changes with respect to uniaxial pressure. Moreover, the accurate measurements of the dihedral angle between the grain contacts are unique attributes, which can be used for understanding the grain growth, anisotropic energetics, and microstructural dimensionality.[13] Although the proposed technique is limited for capturing the surface microstructural features, which may be possibly different from the inside, it indeed provides unexplored insights into the cold sintering process and even enables the characterization of localized phenomena at ceramic and ceramic composite grain boundaries.

Methods

Cold sintering process

ZnO (Alfa Aesar 40–100 nm APS powder) and the transient chemistry of 2 M acetic acid solution were cold-sintered for 60 minutes of isothermal dwell at 200 °C after an average heating rate of 15 °C min^{-1} at various hydraulic uniaxial pressures (70, 205, 340, and 475 MPa). The detailed experimental procedure is described in the previously reported work.[14] To obtain a very flat in-plane surface using atomic force microscopy (AFM) measurement, a finely polished inconel disk (Nickel Alloy 625) was inserted between the powder layer and die punch to preserve the pristine microstructural features

such as the grain, grain boundary, and pore. It should be noted that this proposed method does not require the use of thermal or chemical etching to reveal a grain groove and can be generally applicable to other cold sintering material systems for characterizing topographic features and localized mechanical and electronic phenomena. The commercially available inconel disk (McMaster-Carr 625 Nickel) was cut from a 3.175 mm thick sheet using electrical discharge machining and then polished using alumina suspension.

AFM characterization

An AFM (Bruker Dimension Icon II) and a probe (Bruker SCANASYST-AIR) were used in PeakForce tapping mode to characterize the topographies of the cold-sintered sample. After image flattening and filtering processes, topographic analysis was conducted using a custom MATLAB file (https://github.com/sunhwibang/AFMtopographygithub.com/sunhwibang/AFMtopography), which takes (x, y, z) coordinates as the input and extracts the surface dihedral angle (ψ), peak-to-peak distance (d) and height (h) as the output. Then, the ratio of the grain boundary energy (γ_{GB}) and surface free energy (γ_s) is related to ψ by using Mullins analysis:[15]

$$\frac{\gamma_{GB}}{\gamma_s} = 2\cos\left(\frac{\psi}{2}\right) \quad (1)$$

To achieve a statistically significant data size, 550 grain boundaries were randomly analyzed for each uniaxial pressure.

Results

Surface microstructure

Fig. 1a demonstrates an example of the grain-to-grain contact of the cold-sintered ZnO by the AFM height measurement. The 3D topography clearly displays the distinction between the grain and grain boundary and the roughness between the two grains, which may be due to the grain shape accommodation under the given cold sintering conditions. On the 2D line plot, a peak is defined as the highest point seen from the valley, the height is the distance between the average peak to valley, and the dihedral angle (ψ) is the groove angle measured between two peaks. Fig. 1b–e shows the microstructures at various uniaxial pressures. At 70 MPa, it is evident that a wide range of grain sizes is shown from 50 to 800 nm, indicating that some of the initial particle is still present in the microstructure while the grain growth was in progress. Also, the presence of the anisotropic grain is clear, suggesting that the pressure may impact the growth rate during heating and isothermal dwell (Fig. S1, ESI†). This observation agrees with the previously reported study[16] in which the grain aspect ratio increases at a low pressure (27 MPa). In the cases of 205 and 340 MPa, the population of the initial size is no longer observed and the grain growth is rather equiaxed. It is not yet clear the role of the uniaxial pressure with respect to the grain growth, but these pressures may improve the homogeneous transient phase distribution between grain contacts, which will determine the

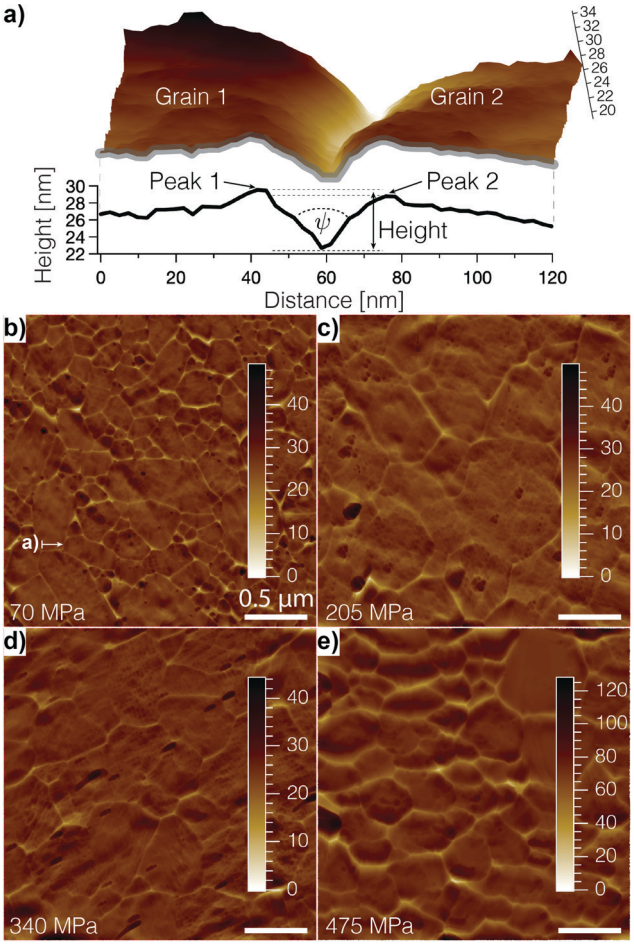

Fig. 1 AFM height measurements (nm) of the cold-sintered ZnO at 200 °C for 60 minutes. (a) 3D groove of adjoining grains viewed from the arrow shown on b) and the bottom plot displays the cross-section of the highlighted region, including the peak, average height, and surface dihedral angle (ψ). (b–e) Various uniaxial pressures of 70, 205, 340, and 475 MPa.

rates of dissolution and precipitation. Regarding the surface flatness of these pressures (70–340 MPa), the maximum height is below 45 nm, which sufficiently captures the in-plane microstructural features without undesired distortion from surface roughness. However, when 475 MPa is used, the maximum height now increases to 125 nm, which is due to the sharp increase in height between the grain contacts. As the size and shape of the grain are changed to larger and faceted compared with the initial particle observed in the case of 70 MPa, the high pressure still has mechanochemical effects but the particle growth mechanism may be different from the low pressures.

Topographic analysis

Fig. 2a plots the histograms of the surface dihedral angles. At 70 and 475 MPa, a bell curve is centered around 90 °C, whereas the cases of 205 and 340 MPa apparently show a negatively skewed distribution where the modes are placed between 130 and 140 °C. This supports the aforementioned microstructural observations where the growth kinetics may be

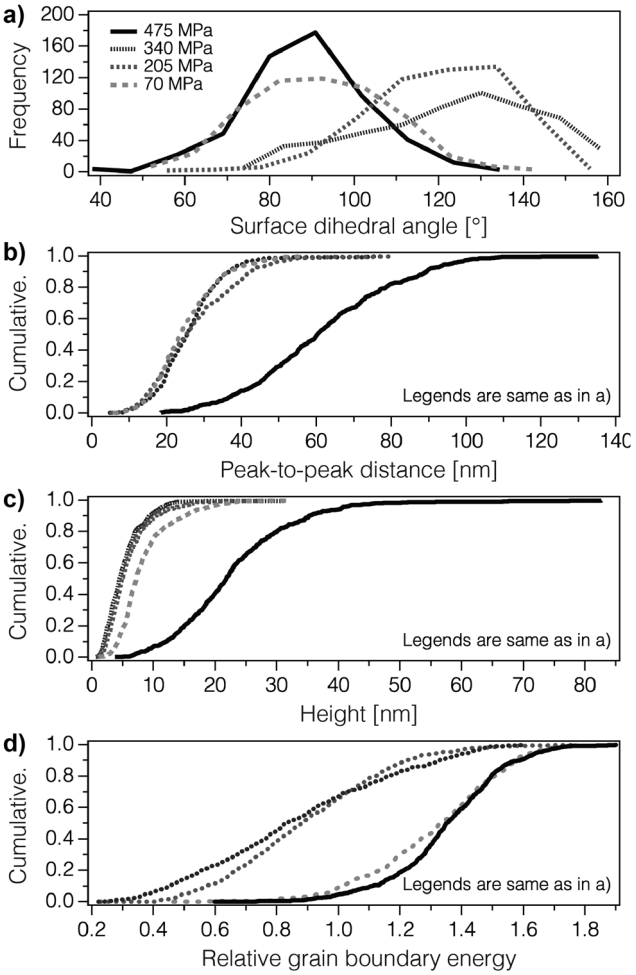

Fig. 2 Topographic analysis of 550 data points at different applied pressures. (a) Surface dihedral angle distributions between adjoining grains. Cumulative frequencies of the (b) peak-to-peak distance, (c) height, and (d) relative grain boundary energy using eqn (1).

distinctively different based on the applied pressure. Considering that two contacting spheres make a 90° angle between zeniths, it can be reasonably deduced that the length of the interparticle contact may be smaller in the cases of 70 and 475 MPa compared with the larger dihedral angle. Fig. 2b and c measure the cumulative frequencies of the peak-to-peak distance and height. For 70–340 MPa, the median (50%) of the peak-to-peak distance is 24.7 ± 1.1 nm, but the height is noticeably reduced by 60%. Then, maintaining the same groove width while shortening the height leads to a conclusion that the growth of the interparticle contact is clear for the cases of 205 and 340 MPa. Although these low pressures present a comprehensible microstructural trend between the interparticle contact growth and applied pressure, the case of 475 MPa shows different growth behaviors. The corresponding median values of its width and height measurements are 60.1 and 21.8 nm, respectively. Considering all the topographic observations of the high pressure case, it is plausible that the ZnO particles are prone to a coarsening process where the grain shape changes due to the confined space defined by the die dimensions.

For the case of ZnO cold sintering with acetic acid solvent, it has been widely reported that zinc acetate appears as one of the possible transient phases,[14] which can thermally decompose and recrystallize to form ZnO:

$$Zn(CH_3COO)_2 + H_2O \rightarrow ZnO + 2CH_3COOH \quad (R1)$$

As the current study uses the sintering temperature of 200 °C, it is likely that the zinc acetate phase still remains in the system regarding its differential thermal analysis data.[17] Then, with the residual zinc acetate, this coarsening may share some perspectives reported in the literature.[18] Fig. 2d displays the relative grain boundary energy based on eqn (1) and the two major median values are 0.85 ± 0.03 and 1.34 ± 0.01. It should be noted that the relative grain boundary energy is equal to unity when the surface surface dihedral angle is 120°, which is the same angle observed in the 2D triple junction with isotropic energies. Table 1 summarizes topographic analysis and the relative grain boundary energy of the current study and compares with other relative grain boundary energy studies using thermal etching. Comparing the normal grain growth cases of the cold-sintered ZnO (205–340 MPa), the peak-to-peak distance is at least one order of magnitude smaller than the thermal grooves, whereas both the surface dihedral angle and relative grain boundary energy are in reasonable agreement.

Discussion

Pressure-dependent geometric model

From topographic analysis, it is evident that the applied pressure changes the resulting geometry of adjoining grains. In order to understand such a pressure-dependent phenomenon, it is important to know the different pressures present during a cold sintering process. When an external uniaxial pressure is applied, the resulting radial die wall pressure is linearly proportional, which can be denoted as:

$$P_{radial} = KP_{axial}, \quad (2)$$

where K is the coefficient pertaining to particle compaction behaviors and its typical value is 0.46 ± 0.04.[24] It should be noted that these pressures have concerns in ceramic powders, metal compaction, and pharmaceutical pill pressing. Across these different fields, there is a general agreement on the presence of the uniaxial and radial pressures, where the radial component is linked to particle friction and friction from the die wall.[25,26] However, the localized particle pressure can be

Table 1 Summary of the peak-to-peak distance (d), surface dihedral angle (ψ), and relative grain boundary energy (γ_{GB}/γ_s)

Materials	d [nm]	ψ [°]	γ_{GB}/γ_s @ 50%
ZnO (current study)	25–27	128–131	0.82–0.88
Magnesia[19]	2000–2200	105	1.22
Alumina[20]	307–327	116–120	1.00–1.05
Na_2O_3-doped alumina[21]	964–1260	123–133	0.80–0.95
Ca-doped yttria[22]	400–470	156–164	0.28–0.42
YAG[23]	350–370	155–160	0.35–0.52

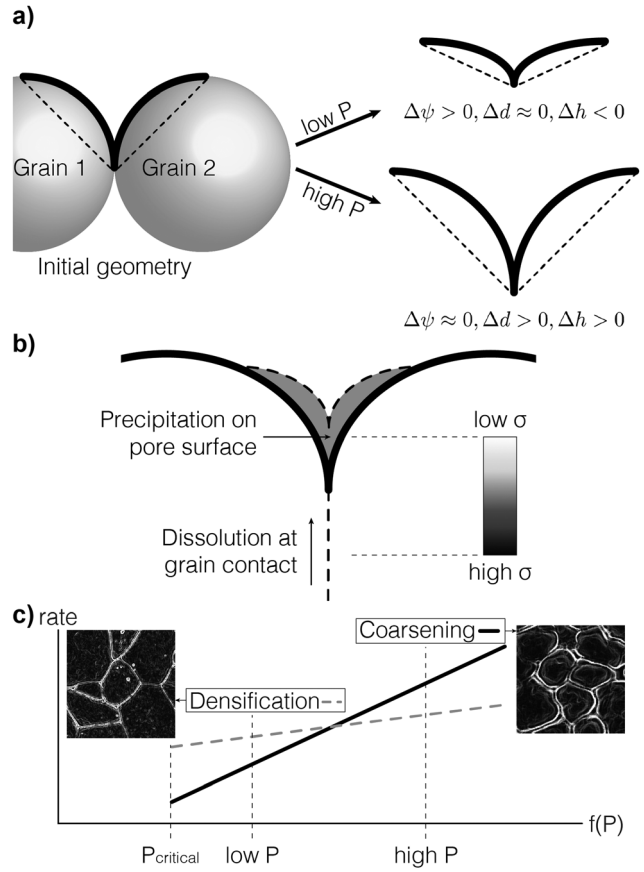

Fig. 3 (a) Adjoining grain geometry evolves with respect to applied pressures changing the dihedral angle (ψ), peak-to-peak distance (d), and height (h). (b) Pressure-solution creep of adjoining grains under applied pressures where dissolution occurs at the grain contact and precipitation occurs at the pore surface and the mass transport follows the local stress gradient (σ). (c) Rates of densification and coarsening depend on the applied pressure where $P_{critical}$ is a minimal pressure to drive sintering phenomena.

distinctively different from the axial and radial global pressures as the Hertz contact theory is now considered to describe the stress between adjoining surfaces.[27] Also, the capillary force is presented in a powder-solvent system where a thin liquid bridge can pull the adjoining spheres and the nano-range separation distance can result in the exponential force effect.[28] Hence, we recognize that both global and localized pressures are present during a course of ZnO cold sintering, but the localized pressure will be highly variable due to the rapid change in the particle morphology and evaporation of the transient phase, which contributes to a thermodynamic non-equilibrium nature of the cold sintering.

Fig. 3a demonstrates the grain geometric model based on the topographic measurements. Assuming that the initial geometry of adjoining grains consists of the point contact, in the case of low pressures, such a point contact evolves into a line contact due to particle coalescence, resulting in a wider dihedral angle and shorter height while the peak-to-peak distance remains the same. In contrast, a high pressure is more relatable to particle coarsening in a confined space where the point contact is still maintained while both the height and peak-to-peak distance increase. Considering the pressure-solution creep as a dominant mechanochemical reaction that drives a cold sintering process, the proposed geometric model is also explainable by its dissolution and precipitation along with the stress potential. Fig. 3b describes that solvent-enhanced dissolution occurs at the grain contact and the dissolved species move along the localized pressure gradient and then precipitate on the closest pore surface. Both particle coalescence and Ostwald ripening may play a key role to obtain sintering; once amorphous crystals form on the pore surface *via* Ostwald ripening, then these new phases recrystallize onto neighboring particle surfaces *via* particle coalescence to minimize the interfacial free energy.[29] Fig. 3c conceptualizes the pressure-dependent sintering phenomena. Letting the critical pressure ($P_{critical}$) be defined as the minimal global pressure to drive cold sintering, this study finds that the different applied pressure does seem to have an impact on either densification or coarsening. Considering that particle coarsening is driven by Ostwald ripening,[30] this implies that the high pressure accelerates Ostwald ripening where the recrystallization becomes a rate-limiting step.

Estimating the absolute grain boundary energy

From the given relative grain boundary energy measurements, the absolute grain boundary energy can be estimated if the surface free energy is known, which can be experimentally characterized using Young's equation:

$$\gamma_{sv} = \gamma_{sl} + \gamma_{lv}\cos\theta, \quad (3)$$

where γ_{sv}, γ_{sl} and γ_{lv} are the interfacial surface tension between solid–vapor, solid–liquid and liquid–vapor phases, respectively. Here, θ refers to the thermodynamic equilibrium of these interfaces and it is inversely proportional to the surface free energy.[31] Table 2 summarizes the wide range of ZnO surface free energies in the literature as they can be highly dependent on the crystal direction, particle size, morphology, roughness, and hydration confined between surfaces. Among the wide range of surface free energies, the case of water confinement may be closely relevant to the pressure solution creep model as the existence of a thin fluid film controls the interface reaction and deformation kinetics.[32] Then, regarding eqn (1) and relative grain boundary energy measurements, the absolute grain boundary energy of the cold-sintered ZnO is estimated to be small as well, which may closely explain the fast and low-temperature nature of cold sintering. This view agrees with

Table 2 Summary of the experimental and theoretical calculations of the contact angle (θ) and surface free energy (γ_{sv}) of ZnO

θ [°]	γ_{sv} [J m^{-2}]	Comment
81 ± 4	0.039 ± 0.003	Surface roughness of 175 nm[34]
132–154	N/A	Thin film fabricated using (R1)[35]
N/A	4.0	Cleavage energy along *c* axis[36]
N/A	2.3	Cleavage energy for (1010) surface[36]
N/A	1.31 ± 0.07	Hydrated nanoparticle surface[37]
N/A	2.55 ± 0.23	Anhydrous nanoparticle surface[37]
N/A	0.015–0.053	Water confined between surfaces[38]

the grain growth energetic study where the activation energy is only 20% of conventional ZnO sintering.[33]

Conclusions

Although the in-plane microstructure contains distinct information compared to fractography, obtaining a highly flat surface while preserving the microstructural features of a cold-sintered sample has been a challenge. Taking ZnO as the model sintering system, this study proposes a method of preserving the flat and pristine surface microstructure for understanding topographic evolutions at various pressures. Using low pressures (70–340 MPa), the interparticle contact was clearly growing while keeping a similar groove geometry. However, a high pressure (475 MPa) rather promotes particle coarsening under a confined space. These observations present that the rates of densification and coarsening depend on uniaxial pressures, which can be an important consideration in controlling the microstructure and associated properties. As the surface dihedral angle is a unique morphological attribute, accurate measurements on the preserved in-plane microstructure certainly contribute to the in-depth understanding of the grain growth kinetics and anisotropic energetics of a cold sintering process.

Conflicts of interest

There are no conflicts to declare.

Acknowledgements

We would like to acknowledge generous support from the National Science Foundation (DMR-1728634) for enabling the fundamental cold sintering study. We also greatly appreciate the AFM discussion with Mr Teague Williams from the Penn State Materials Research Institute and the research staff from the Materials Characterization Laboratory.

Notes and references

1 Z. L. Wang, *J. Phys.: Condens. Matter*, 2004, **16**, R829.
2 S. C. Pillai, J. M. Kelly, R. Ramesh and D. E. McCormack, *J. Mater. Chem. C*, 2013, **1**, 3268–3281.
3 S. Pearton, D. Norton, K. Ip, Y. Heo and T. Steiner, *Superlattices Microstruct.*, 2003, **34**, 3–32.
4 B. Dargatz, J. Gonzalez-Julian and O. Guillon, *Sci. Technol. Adv. Mater.*, 2015, **16**(2), 025008.
5 C. A. Randall, J. Guo, A. Baker, M. Lanagan and G. Hanzheng, *Cold sintering ceramics and composites*, 2017, US Patent App. 15/277,553.
6 A. Serrano, O. Caballero-Calero, M. Á. Garca, S. Lazi, N. Carmona, G. R. Castro, M. Martn-González and J. F. Fernández, *J. Eur. Ceram. Soc.*, 2020, **40**, 5535–5542.
7 C. Spiers and P. Schutjens, *Oil Gas Sci. Technol.*, 1999, **54**, 729–750.
8 A. Ndayishimiye, M. Y. Sengul, S. H. Bang, K. Tsuji, K. Takashima, T. H. de Beauvoir, D. Denux, J.-M. Thibaud, A. C. van Duin and C. Elissalde, *et al.*, *J. Eur. Ceram. Soc.*, 2020, **40**, 1312–1324.
9 Y. Yong, M. T. Nguyen, T. Yonezawa, T. Asano, M. Matsubara, H. Tsukamoto, Y.-C. Liao, T. Zhang, S. Isobe and Y. Nakagawa, *J. Mater. Chem. C*, 2017, **5**, 1033–1041.
10 T. H. de Beauvoir, A. Sangregorio, I. Cornu, C. Elissalde and M. Josse, *J. Mater. Chem. C*, 2018, **6**, 2229–2233.
11 A. Ndayishimiye, M. Y. Sengul, D. Akbarian, Z. Fan, K. Tsuji, S. H. Bang, A. C. Van Duin and C. A. Randall, *Nano Lett.*, 2021, **21**, 3451–3457.
12 J. Gonzalez-Julian, K. Neuhaus, M. Bernemann, J. P. da Silva, A. Laptev, M. Bram and O. Guillon, *Acta Mater.*, 2018, **144**, 116–128.
13 E. A. Holm and M. E. Chandross, Determination of Dihedral Angles at Grain Boundary Triple Junctions., *Sandia national lab.(snl-nm), albuquerque, nm (united states) technical report*, 2010.
14 S. H. Bang, A. Ndayishimiye and C. A. Randall, *J. Mater. Chem. C*, 2020, **8**, 5668–5672.
15 W. W. Mullins, *J. Appl. Phys.*, 1957, **28**, 333–339.
16 S. H. Bang, K. Tsuji, A. Ndayishimiye, S. Dursun, J. H. Seo, S. Otieno and C. A. Randall, *J. Am. Ceram. Soc.*, 2020, **103**, 2322–2327.
17 T. Arii and A. Kishi, *Thermochim. Acta*, 2003, **400**, 175–185.
18 B. Dargatz, J. Gonzalez-Julian and O. Guillon, *J. Cryst. Growth*, 2015, **419**, 69–78.
19 D. M. Saylor and G. S. Rohrer, *J. Am. Ceram. Soc.*, 1999, **82**, 1529–1536.
20 M. N. Kelly, S. A. Bojarski and G. S. Rohrer, *J. Am. Ceram. Soc.*, 2017, **100**, 783–791.
21 S. J. Dillon, M. P. Harmer and G. S. Rohrer, *J. Am. Ceram. Soc.*, 2010, **93**, 1796–1802.
22 S. A. Bojarski, S. Ma, W. Lenthe, M. P. Harmer and G. S. Rohrer, *Metall. Mater. Trans. A*, 2012, **43**, 3532–3538.
23 S. J. Dillon and G. S. Rohrer, *Acta Mater.*, 2009, **57**, 1–7.
24 K. Yanai and M. Hirai, *J. Jpn. Soc. Powder Powder Metall.*, 2000, **47**, 353–363.
25 S.-T. Hong, Y. Hovanski, C. A. Lavender and K. S. Weil, *J. Mater. Eng. Perform.*, 2008, **17**, 382–386.
26 S. Abdel-Hamid and G. Betz, *Drug Dev. Ind. Pharm.*, 2011, **37**, 387–395.
27 M. Machado, P. Moreira, P. Flores and H. M. Lankarani, *Mech. Mach. Theory*, 2012, **53**, 99–121.
28 Y. I. Rabinovich, M. S. Esayanur and B. M. Moudgil, *Langmuir*, 2005, **21**, 10992–10997.
29 M. Y. Sengul, J. Guo, C. A. Randall and A. C. van Duin, *Angew. Chem.*, 2019, **131**, 12550–12554.
30 P. W. Voorhees, *J. Stat. Phys.*, 1985, **38**, 231–252.
31 W. J. Khudhayer, R. Sharma and T. Karabacak, *Nanotechnology*, 2009, **20**, 275302.
32 R. van Noort, H. J. M. Visser and C. J. Spiers, *J. Geophys. Res.*, 2008, **113**, B03201.
33 S. Funahashi, J. Guo, H. Guo, K. Wang, A. L. Baker, K. Shiratsuyu and C. A. Randall, *J. Am. Ceram. Soc.*, 2017, **100**, 546–553.
34 L. D. Trino, L. F. Dias, L. G. Albano, E. S. Bronze-Uhle, E. C. Rangel, C. F. Graeff and P. N. Lisboa-Filho, *Ceram. Int.*, 2018, **44**, 4000–4008.

35 N. Tarwal and P. Patil, *Appl. Surf. Sci.*, 2010, **256**, 7451–7456.
36 A. Wander, F. Schedin, P. Steadman, A. Norris, R. McGrath, T. Turner, G. Thornton and N. Harrison, *Phys. Rev. Lett.*, 2001, **86**, 3811.
37 P. Zhang, F. Xu, A. Navrotsky, J. S. Lee, S. Kim and J. Liu, *Chem. Mater.*, 2007, **19**, 5687–5693.
38 X. Zhang, Z. Shen, J. Liu, S. Kerisit, M. Bowden, M. Sushko, J. De Yoreo and K. M. Rosso, *Nat. Commun.*, 2017, **8**, 1–8.